Determination of the Spatial Extent of the Engine Exhaust-Disturbed Region of the Chang'E-4 Landing Site Using LROC NAC Images

Yaqiong Wang, Huan Xie 🆔, *Senior Member, IEEE*, Chao Wang 🆔, Xiaohua Tong 🆔, *Senior Member, IEEE*, Sicong Liu 🆔, *Member, IEEE*, and Xiong Xu 🆔, *Member, IEEE*

Abstract—The regolith of the Chang'E-4 landing site was disturbed by its engine exhaust. To explore the interaction between the engine exhaust and the regolith, it was necessary to identify the exhaust-disturbed region. This article focuses on determining the extent of the disturbed region by using lunar reconnaissance orbiter camera narrow angle camera (LROC NAC) images. For this purpose, the tools of temporal-ratio images, phase-ratio images, reflectance profiles, and reflectance isoline graphs are employed. The reflectance profiles and isoline graphs derived from the temporal-ratio images reveal the reflectance changes before and after landing. Compared with the reflectance profiles, isoline graphs further include the spatial information of isolines, thus more robust to noise. Based on the magnitudes of changed reflectance around the lander, the engine exhaust-disturbed region was further divided into the focus disturbed region (FDR) and the diffuse disturbed region (DDR). The final estimated spatial extent along the north–south and east–west directions of the FDR were ∼9.6 and ∼10.8 m, and those of the DDR were ∼75 and ∼80 m. As compared with the estimated spatial extent of the Chang'E-3 landing site, the DDR of the Chang'E-4 landing site was larger, but the FDR was smaller. We attributed this to geological and topography factors. The reflectance changes between the FDR and the undisturbed region increased by ∼10±1%. This indicates similar processes causing the variations in the regolith properties, likely including the smoothing of the surface from microscopic to macroscopic by destroying fine-grained regolith components, or changing of the surface maturity.

Index Terms—Engine exhaust disturbance, remote sensing tool, spatial extent.

Yaqiong Wang and Huan Xie are with the College of Surveying and Geo-Informatics, Tongji University, Shanghai 200092, China, and also with the Shanghai Key Laboratory of Space Mapping and Remote Sensing for Planetary Exploration, Shanghai 20092, China (e-mail: 1810655@tongji.edu.cn; huanxie@tongji.edu.cn).

Chao Wang is with the College of Surveying and Geo-Informatics, Tongji University, Shanghai 200092, China, also with the Shanghai Key Laboratory of Space Mapping and Remote Sensing for Planetary Exploration, Shanghai 20092, China, and also with the Shanghai Institute of Intelligent Science and Technology, Shanghai 20092, China (e-mail: wangchao2019@tongji.edu.cn).

Xiaohua Tong, Sicong Liu, and Xiong Xu are with the College of Surveying and Geo-Informatics, Tongji University, Shanghai 200092, China (e-mail: xhtong@tongji.edu.cn; sicong.liu@tongji.edu.cn; xvxiong@tongji.edu.cn).

Digital Object Identifier 10.1109/JSTARS.2022.3227364

I. INTRODUCTION

LUNAR regolith is a layer of powder-like substance, in which its physical properties, composition, and structure directly affect its reflectance [1], [2]. The reflectance variations can be characterized by photometry. Different photometric properties indicate different regolith properties. By analyzing the photometric properties, information about the regolith such as regolith particles' shape, size, composition, and structure can be derived [2], [3], [4]. Based on previous studies, in terms of the Surveyor, Luna, and Apollo spacecraft landing sites, the reflectance changes between the engine exhaust disturbed regions and the UDR are still visible in some specific lunar reconnaissance orbiter camera narrow angle camera (LROC NAC) images with a resolution of 0.5–2 m/pixel [4], [5]. These reflectance anomalies have been interpreted as the regolith properties of the landing site surface that were disturbed by the engine exhaust during the lander's descent and some of them are also disturbed by the activities of rovers and astronauts around the landers [4], [5], [6], [7]. Measurements derived from the in situ reflectance spectra of the Moon acquired by the visible-near infrared spectrometer (VNIS) onboard the Chang'E-3 rover revealed that the finest highly weathered particles were removed by engine exhaust [8], [9]. In Chang'E-4 landing site, the photometric abnormal was also observed. Analyzing these photometric properties is helpful for us to understand how the engine exhaust disturbed the regolith properties. For this purpose, the spatial extent of the engine exhaust-disturbed region should be first determined.

According to previous studies [6], [7], for some landing sites, such as Chang'E-3 landing site, the exhaust-disturbed region can be further divided into the focused disturbed region (FDR) and diffuse disturbed region (DDR) according to the magnitude of reflectance change. The FDR is a region that was severely disturbed while the DDR is a diffuse area around the FDR, whose reflectance also shows some anomalies but is not as obvious as the FDR. And the reflectance profile is a useful tool to qualify the reflectance changes [5], [6], [7]. It should be noted that the DDR can not be distinguished in all the landing sites, such as Apollo landing missions. In terms of the Apollo, Surveyor, and Luna landing missions, their spatial measurements for the disturbed region mainly used the LROC NAC images and the derived phase-ratio images [4], [7]. The phase-ratio image

essentially characterizes the phase function slope [10], [11]. The phase-function slope partly indicates the regolith roughness and illumination-scattering characteristics and it can be measured by phase ratio for a pair of phase angles. In the phase-ratio image, a darker region corresponds to a lower phase slope [10], [12]. The photometric anomalies, observed from the phase-ratio image, reveal the possible anomalies of a lunar regolith [5], such as variation of regolith maturity, smoothing of small-scale surface topography on mm to cm scales, destruction of the "fairy-castle" structures, and so on. In addition, according to the VNIS detection, the dominant impact of the engine exhaust disturbance is considered to be the blowing away of the uppermost fine regolith. As a result, the regolith in the disturbed region will have a larger particle size than that in the undisturbed area. In addition, it reveals that the remaining regolith in the disturbed regions was less space weathered [8], [13].

The phase-ratio image has proven to be a reliable tool to detect photometric anomalies and indicating the regolith property changes [4], [5], [6], [7], [11]. In particular, the reflectance contrast of the disturbed region and the undisturbed region (UDR) is enhanced in the phase-ratio image, thus providing an opportunity to determine the spatial extent of the disturbed region. However, this kind of spatial measurement is largely dependent on the visual interpretation of the phase-ratio image. While the presence of the phase-ratio image is affected by topographic factors, such as meter-level craters, meter-level low-lying, and so on. As a result, the final determination of the spatial extent based on the phase-ratio image is subjective and qualitative. In addition, reflectance profiles are further introduced for a more reliable spatial extent measurement [4], [6]. Based on LROC NAC images or phase-ratio images, reflectance profiles quantify the reflectance changes along certain directions or extension paths defined in advance. Due to the reflectance profile path being a line (i.e., straight or curved), in terms of the whole landing site, the available information on the reflectance profile is limited. In addition, it is inevitable that some topographic effects will be included in the profile. As a result, the determination of the spatial extent by using the reflectance profile is not reliable.

This study considered the aforementioned challenges, and temporal-ratio images and isoline graphs were used for the determination of the spatial extent of the Chang'E-4 lander's engine exhaust-disturbed region. LROC NAC images with a range of various incidence and emission angles of the Chang'E-4 landing site, both before and after landing, are available. The temporal-ratio image, which is the ratio of the images before and after landing, has proven to be an efficient tool for determining the spatial extent of the engine exhaust-disturbed region [6]. When ignoring issues such as various illumination conditions, terrain, and image registration errors, in theory, the ratio value of the UDR in the temporal image should be 1.0 while the ratio value of the engine exhaust-disturbed region should be away from 1.0; therefore, based on this regulation, the spatial extent of the engine exhaust-disturbed region can be delimited. The isoline graph is a tool that is applied to determine the spatial extent of the engine exhaust-disturbed region. In this article, the isoline graph was derived based on the temporal-ratio images. As compared to the reflectance profile, which can only use local information of the ratio image, the isoline graph considers the information of the whole landing site and describes the continuous, gradual changes in the ratio values.

Analyzing the photometric anomalies of the landing site based on the NAC images allowed us to study the lunar regolith properties by using a remote sensing tool. These results have been expanded with in situ data-based results [14], [16]. Scientific payloads equipped with the rover have obtained the in situ data, and research analyzing regolith properties according to these data are ongoing [17], [18]. In this study, we focused on using a temporal-ratio image and isoline graph to determine the spatial extent of the engine exhaust-disturbed region, and the phase-ratio images and reflectance files were used for cross-evaluation. In addition, a phase-ratio image was also used to infer the possible causes of the photometric anomalies.

II. DATA AND METHOD

The Chang'E-4 spacecraft landed on the Von Kármán crater at 177.59° E, 45.46° S, on the lunar's far side on January 3, 2019 [19]. LROC NAC images at various resolutions observed the landing, and illumination geometries of this landing site were captured both before and after the landing. Based on these images, phase-ratio images and temporal-ratio images were derived. To obtain reliable ratio images, NAC images were first preprocessed. In our work, we mainly used the United States Geological Survey Integrated Software for Imagers and Spectrometers [20], [21] to conduct the image format conversion, denoising, reflectance (I/F) calibration, photometric correction, and map projection. Image matching was manually performed with the MATLAB image registration tool [22]. I/F represents the radiance factor, which was defined as the ratio of the radiance (I) to the irradiance (F) from a normally illuminated Lambertian surface [21], [5].

A. Temporal-Ratio Images

Temporal-ratio images mapped the quotient of the image pair before and after the Chang'E-4 lander touched down. The temporal-ratio image directly revealed the reflectance change of the landing site, indicating a regolith disturbance caused by the spacecraft engine exhaust. In the temporal-ratio image, the disturbed area was highlighted, and in theory, the temporal-ratio image was immune to topological factors since both identical illumination conditions and observing viewings were required for the image pair. As a result, the spatial extent of the disturbed area could be accurately determined. In practice, the images used for making temporal-ratio images may have slight differences in incidence angles and emission angles, and therefore, some noises such as terrain influences and matching errors can exist in the resultant temporal-ratio images. In addition, although these images have been pre-processed by reflectance (I/F) calibration, photometric correction, and map projection, all these can introduce errors in each image. However, when making the ratio image, the influence of these errors is much smaller than it of image lighting conditions and topography factors. Therefore, in this article, errors introduced by image lighting conditions differences and topography factors are mainly considered.

TABLE I
PHOTOMETRIC AND ILLUMINATION GEOMETRIC CHARACTERISTICS OF THE SELECTED LROC NAC IMAGES OF CHANG'E-4 LANDING SITE USED TO CREATE THE TEMPORAL-RATIO IMAGE

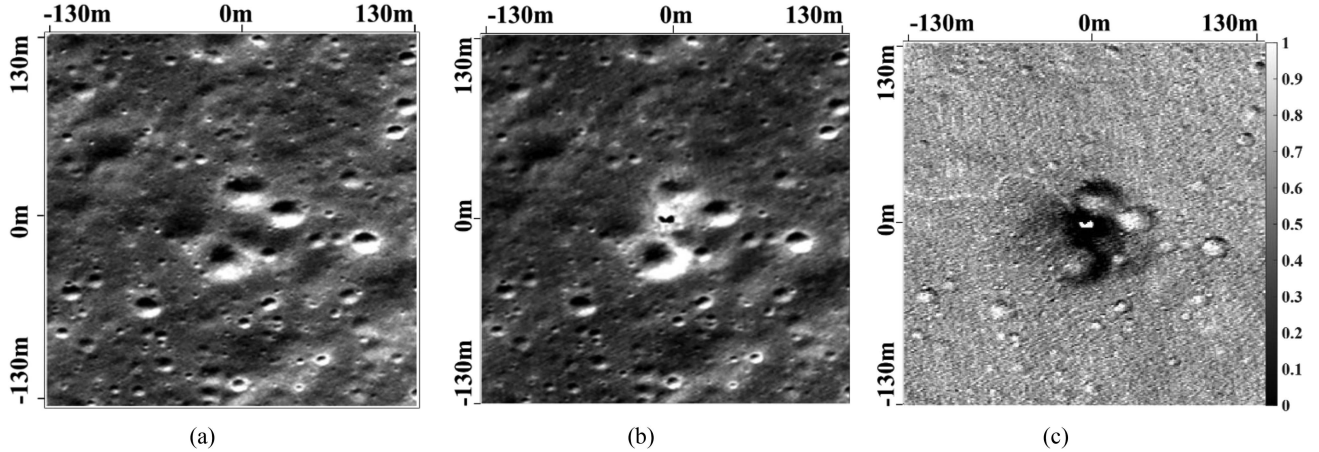| Image ID	Captured Time	Resolution (m/pixel)	Incidence angle (°)	Emission angle (°)	Phase angle (°)	Sub-solar latitude (°)	Sub-solar longitude (°)
M1298916428L	Before landing	0.772	47.22	1.72	47.72	1.03	169.09
M1372969744R	After landing	0.782	46.07	4.61	47.36	-1.19	163.1

Fig. 1. Pair of LROC NAC images and their derived temporal-ratio images. (a) LROC NAC image M1298916428L prior to the landing. (b) LROC NAC image M1372969744R after the landing. (c) Temporal-ratio image made by dividing M1372969744R by M1298916428L. These images are presented using image-enhancement technology for a better visual effect.

To obtain reliable temporal-ratio images, the following regulations were followed:

1) the image pair was required to have similar incidence and emission angles and would, therefore, have similar phase angles (for all these angles, the difference should be < 5°);
2) the image pair should have similar illumination geometries, including north sub-solar latitude and longitude (the difference should be < 20°, respectively);
3) the image pair should have similar resolutions and sufficiently registered [10].

The study area surrounded the landing site, and the images were cropped to 200 m × 200 m image patches centered on the landing point, which was defined by the center of the Chang'E-4 lander. Considering the small resolution difference among these images, they were further translated into the same size by referencing the higher resolution of the image pair. The MATLAB register tool was first used to obtain pixel-level registration accuracy and then manually adjusted the image patches to obtain subpixel-level registration accuracy. Based on these regulations, a pair of images were selected. The corresponding detailed information of the pair of images is presented in Table I, and these two images and their derived temporal-ratio images are presented in Fig. 1.

B. Phase-Ratio Image

A phase-ratio image is created by mapping the quotient of the two images of the same region; these two images should have similar incidence angles but different phase angles. By dividing the higher phase angle image by the lower, the phase-ratio image is the result. The phase-ratio image measures the slope k of the phase function, $k = g(\alpha_1)/g(\alpha_2)$, where $g(\cdot)$ stands for the phase function, and α_1 and α_2 denote two different phase angles with $\alpha_1 < \alpha_2$. The phase function defined by the photometric conditions (i.e., the incidence angle i, emission angle e, and phase angle α) was sufficient to characterize the surface reflectance [11], [24]. The slope of the lunar phase function was determined by the multiple incoherent scattering and shadow-hiding effects. Therefore, the photometric anomalies revealed by the phase-ratio image indicated the anomalies of the regolith properties. To obtain reliable phase-ratio images, the following regulations were followed:

1) the image pairs should have similar incidence angles (difference < 5°), but different emission angles, and, thus, different phase angles (a difference of at least >10°);
2) the image pairs should have the similar illumination geometries, including north sub-solar latitude and longitude (at least a difference < 20°, respectively);
3) the image pairs should have similar resolutions and be sufficiently registered [4], [7].

In this article, the phase-ratio image was created by using image pairs of the Chang'E-4 lander after landing. Then the photometric anomalies presented in the phase-ratio image can be used for analyzing how the engine exhaust has affected the regolith properties. The concerned region is around the landing site, and the images are cropped to 200 m × 200 m image patches centered on the landing point, which is identified as the center of the Chang'E-4 lander. The image register method

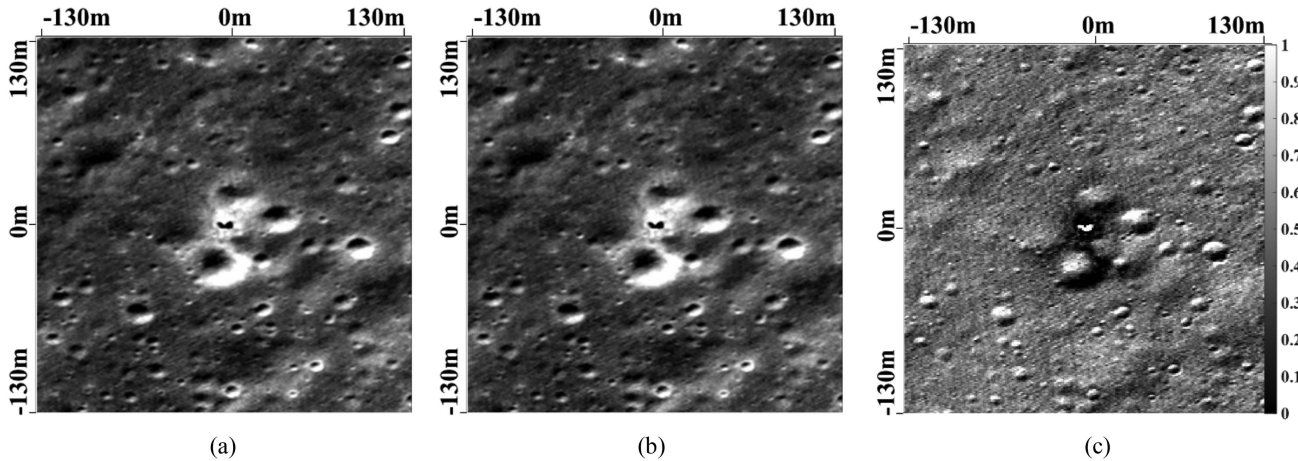| Image ID	Captured Time	Resolution (m/pixel)	Incidence angle (°)	Emission angle (°)	Phase angle (°)	Sub-solar latitude (°)	Sub-solar longitude (°)
M1372969744R	After landing	0.772	47.22	1.72	47.72	1.03	169.09
M1314237625L	After landing	0.823	45.12	30.32	16	-0.93	169.14

Fig. 2. Pair of LROC NAC images and their derived phase-ratio image. (a) LROC NAC image M1372969744R. (b) LROC NAC image M1314237625L. (c) Phase-ratio image made by dividing M1314237625 with M1372969744. These images are presented by using image enhancement technology for a better visual effect.

is the same as Section II-A mentioned. Based on the above-listed regulations, a pair of images is selected. The corresponding detailed information of this pair of images is listed in Table II, and these images and their derived phase-ratio image are shown in Fig. 2.

C. Reflectance Profiles

The reflectance profiles for ratio images quantitatively describe the reflectance changes across a selected region. With a reflectance profile that passed through the landing site, the difference in the reflectance ratio values between the disturbed region and UDR could be qualified. Furthermore, by considering the slope, inflection points, and extreme points of the reflectance profile, the spatial extent of the disturbed area was determined quantitatively along a certain defined reflectance profile path. However, some of the craters and either low-lying or raised regions with resolvable slope changes still showed as artifacts in the phase-ratio image and could also lead to anomalies in the reflectance profiles. As a result, it was difficult to accurately determine whether the anomalies were induced by engine exhaust disturbance or topography.

Based on the ratio images and their corresponding reflectance profiles along each direction, some rules were defined to detect the spatial extent of the FDR and the DDR:

1) uniform fluctuations over a certain range at an approximate value were defined as the I/F ratio for the UDR;
2) an obvious change in the gradient of the curve was defined as the dividing point that distinguished the different regions;

3) if this were in the range of the continuous influence of the engine exhaust, the local anomalous oscillation of the curve caused by topographic factors was ignored.

In this study, the reflectance profiles were drawn along the west–east direction and north–south direction. For a more reliable result for each direction, two profiles were used. Across the west–east, the profiles are respectively denoted as a-a', b-b', and along the north–south direction, the profiles were respectively denoted as c-c', d-d'. Each value of the profile was calculated by averaging the I/F ratio values within a 3×3 window centered on the pixel which had passed through the profile path to minimize the noise effects. In addition, since the reflectance profiles only considered the pixels in a line, the results would heavily fluctuate due to the image noises, which are introduced by terrain influences, image matching errors, and so on, as shown in a later section.

D. Reflectance Isoline Graphs

Isoline graphs derived from the temporal-ratio image reveal reflectance changes of the landing site before and after the spacecraft landing. An isoline graph was composed of a set of isolines, and each of these contours corresponds to a specific ratio value of the temporal-ratio image. In essence, the isoline graph is the result of combing the reflectance profiles of the two-dimensional spatial information, thus it is more effective in determining the spatial extent of the disturbed region.

It is well known that in theory, the reflectance ratio of the undisturbed region should be close to 1.0. However, in practice, the differences in illumination conditions and image resolutions
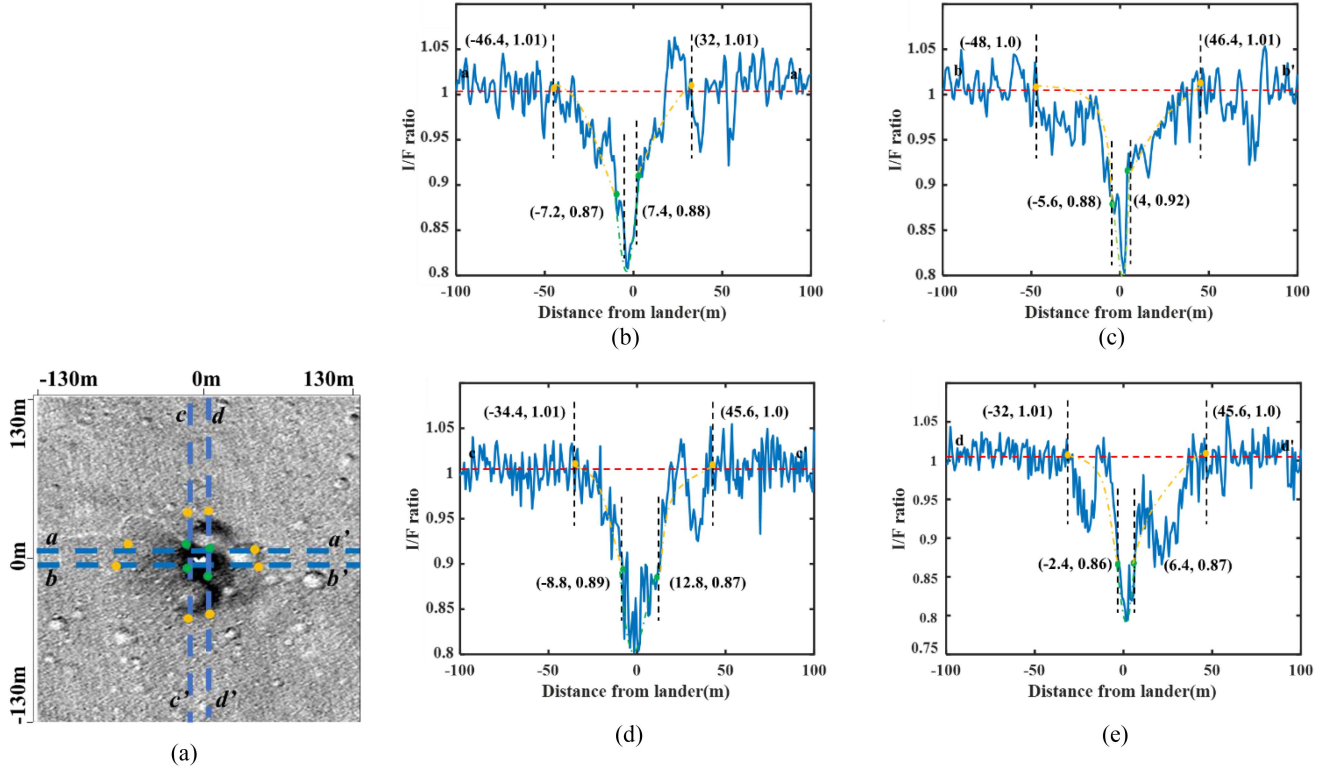
Fig. 3.   Reflectance profiles derived from the temporal-ratio image. (a) Temporal-ratio image; reflectance profile paths are presented as blue dashed lines, and green and blue points denote the image locations of those boundary points derived from the reflectance profiles; corresponding profiles of the paths a-a' (b), b-b' (c), c-c' (d), and d-d' (e) are shown in (a). Red dashed lines in (b)–(e) denote the average I/F values of the UDR where the corresponding profiles pass through. The yellow points highlight the location and reflectance values to distinguish the DDR from the UDR. The green points highlight the boundaries of DDR and FDR.

of the before and after landing images both contributed to the reflectance ratio of the temporal image deviating from 1.0. By further considering the influence of image geometry calibration errors, registration errors, and topographic factors, the reflectance ratio will not necessarily change continuously. As seen in Fig. 4, there are a lot of contours with the same contour level. However, they have spatial distribution continuity. That is from the most severely disturbed region to the undisturbed region, the contour levels (corresponding to I/F ratio) decrease (or increase) from the center to the surroundings. In this way, the boundaries of the disturbed region can be determined by the characteristics of spatial distribution and cumulative frequency of the contours. Let the I/F ratio values vary continuously in an interval, each I/F ratio value corresponds to a set of isolines. In this continuously changing of the I/F ratio values, if the spatial distribution range and the accumulated frequency of the contours suddenly decrease at a certain I/F ratio, then aggregation space of the contours with this I/F ratio covers the disturbed region. In this way, the boundary of the disturbed region is determined. this boundary determination method is applicable to both DDR and FDR. In practice, these series of consecutive contours can be determined by taking the reflectance profiles results as references. Assuming that the reflectance ratio of the disturbed region boundary determined by the reflectance profile is x, then the series of consecutive contours can be determined as $y \subseteq [x\text{-}a\colon b\colon 1.0)$, where $a \in (0.5, x)$, b is the sample interval, and is usually taken as 0.05 or 0.1 in this article. In addition,

if there are no references, then the enumeration method can be employed.

III. RESULTS

A. Spatial Extent Estimation of the Engine Exhaust-Disturbed Region

In this section, spatial extents of FDR and DDR are quantitatively determined by using reflectance profiles and reflectance isoline graphs. First, four reflectance profiles taken across the landing site based on temporal ratio image are employed to delimit spatial extents of FDR and DDR. Then, reflectance isoline graphs are further utilized to determine the spatial extents and cross-validate the results of the reflectance profiles derived.

1) Spatial Extents of FDR and DDR by Using Reflectance (Ratio) Profiles: Previous studies have shown that the profile taken across the temporal-ratio image is a useful tool for identifying the engine exhaust-disturbed region [4], [6]. Here, four profiles respectively across the west–east and north–south directions are utilized to determine the spatial extents along the corresponding directions, and their profile paths are shown in Fig. 3(a). The reported I/F ratio is calculated by dividing I/F after landing by I/F before landing. Notably, the I/F ratio of the undisturbed region should be very close to 1.0. However, the actual derived value in this article is about 0.96. The reasons for this deviation may include residual errors of photometric calibrations, the illumination conditions differences, and the
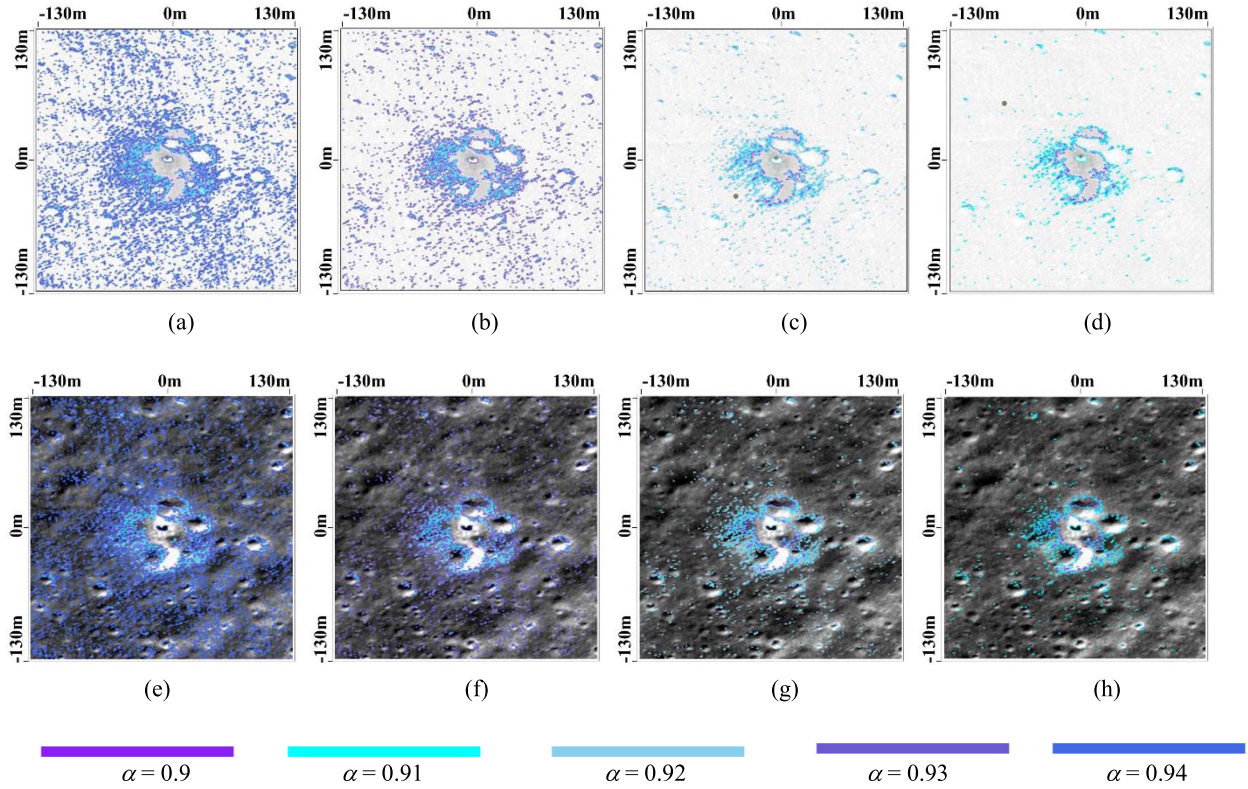
Fig. 4. Isoline graphs of the temporal image using different contour levels. Derived with contour levels. (a) β_1 = {0.94, 0.93 0.92 0.91,0.90}. (b) β_2 = {0.93 0.92 0.91,0.90}. (c) β_3 = {0.92 0.91,0.90}. (d) β_4 = {0.91,0.90}. (e)−(h) are the maps of overlaying the isoline graphs (a)−(d) on the NAC image M1372969744, respectively.

registration errors of both before and after landing images. In fact, this offset does not influence the determination of the spatial extents. Moreover, to illustrate this deviation, necessary multiplicative adjustments are introduced to bring the I/F ratio of the undisturbed region to 1.0 [10]. The profiles shown in Fig. 3 include the adjustment.

Their reflectance profiles are plotted in Fig. 3(b)−(e). As shown in Fig. 3(b) and (c), based on the reflectance profiles a-a' and b-b', the disturbance distances along the west–east direction of the DDR were approximately 78.4 and 94.4 m (the sum of 46.4 and 32 m, and the sum of the 48 and 46.4 m, respectively). The disturbance distances of the FDR were approximately 9.4 and 9.6 m, respectively. As shown in Fig. 3(d) and (e), based on the reflectance profiles c-c' and d-d', the derived disturbed distances along the north–south direction of the DDR were estimated as approximately 80.0 and 77.6 m, respectively. For the FDR, the disturbed distances were estimated as approximately 9.6 and 8.8 m, respectively. We also found that for reflectance profiles themselves, there was a ∼16 m difference along the west–east direction. The reason for this difference was that the performance of the reflectance profiles was easily affected by noise (including topographical factors and register errors) since the reflectance profile could only use the local numerical information along a profile path without the spatial distribution information for the whole landing site.

2) Spatial Extents of FDR and DDR by Using Reflectance (Ratio) Isoline Graphs: Based on the temporal-ratio image and reflectance isoline graphs, the spatial extents of the DDR and the FDR were determined. For determining the spatial extent, a set of contour levels defined by using subsets of β = {0.94, 0.93 0.92 0.91,0.90} were used. Each element in β denotes an I/F ratio calculated as dividing I/F after landing by I/F before landing. As Section II-D illustrated that the elements in β can be determined by using the profiles determined boundary values (for example, the above profile determined I/F ratio value is about 0.95, then we will set elements in around the 0.96 and the finale presented here is the optimal group to illustrate the boundary determination process) or it is possible to experiment a series values and finalize a certain interval, where the finalized interval must cover the I/F ratio of the boundary of DDR and the FDR. The significant characteristic of the boundary I/F ratio is that the frequency of contours changes a lot when compared to other elements cases. From Fig. 4(a) to (d), the isoline graph was derived based on the contour levels of β_1 = {0.94, 0.93, 0.92, 0.91,0.90}, β_2 = {0.93, 0.92, 0.91, 0.90}, β_3 = {0.92, 0.91, 0.90}, and β_4 = {0.91, 0.90}, respectively. By selecting different sets of contour levels, the spatial distributions of the contour levels were also changed. In principle, the reflectance ratio of the undisturbed region was 1.0. However, in practice, the illumination conditions and observed details of the before and after landing images could not be identical. Meanwhile, considering the existence of map registration errors, the reflectance ratio of the undisturbed region was less than 1.0. From Fig. 4(a) to (b), the changed contour level was 0.94, and many of the
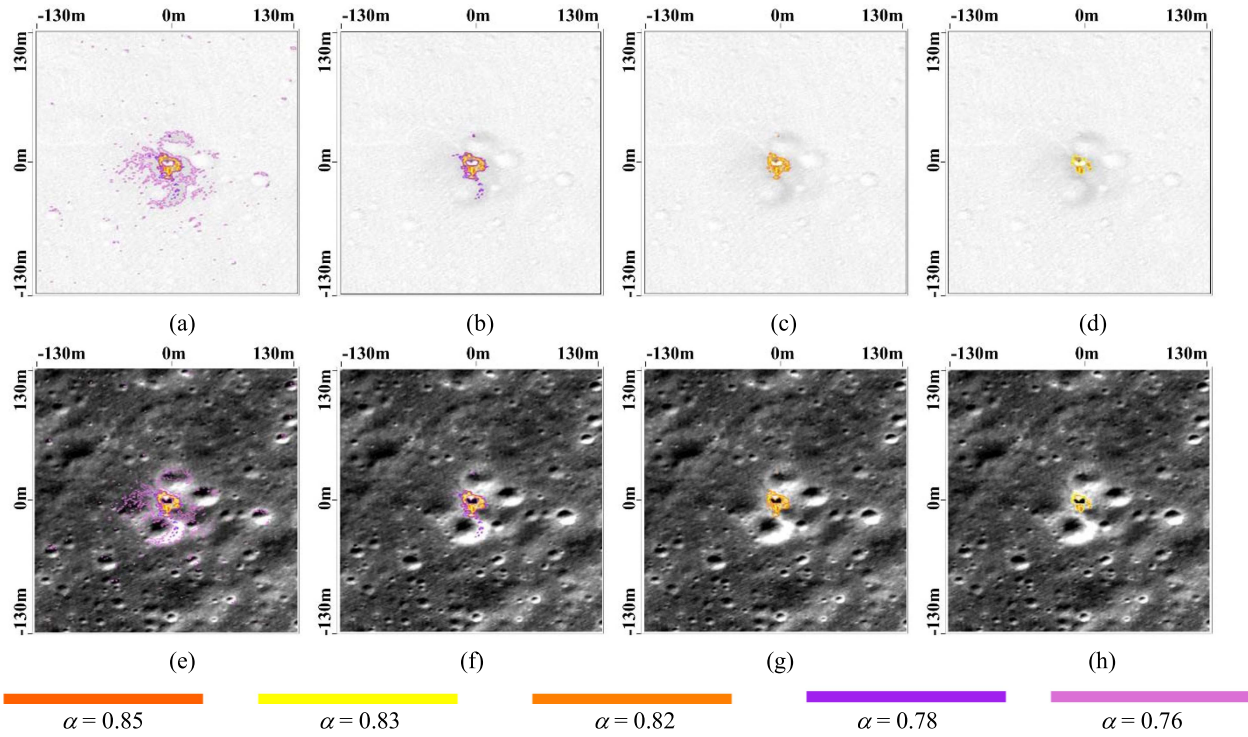
Fig. 5.   Isoline graphs of the temporal image using different contour levels. Derived with contour levels. (a) {0.85, 0.83 0.82 0.80, 0.78}. (b) $\beta_2 = \{0.83\ 0.82\ 0.80, 0.78\}$. (c) $\beta_3 = \{0.82\ 0.80, 0.78\}$. (d) $\beta_4 = \{0.80, 0.78\}$. (e)−(h) are the isoline graphs (a)−(d) mapped on the NAC image M1372969744, respectively.

discretely distributed isolines had disappeared, which indicated that the isolines with a contour level of 0.94 belonged to the UDR. According to Fig. 4(b) and (c), by eliminating the contour level of 0.93, more discrete distributed isolines also disappeared. From Fig. 4(a) to (c), the isolines around the landing site showed an obvious high-density aggregation distribution, which was in sharp contrast to the discrete isolines that were located farther away from the lander. From Fig. 4(c) to (d), the contour level of 0.92 was eliminated, and the high-density cluster region began to shrink. The changes in the spatial distributions of these isolines and their corresponding regions in the NAC images are shown in Fig. 4(e)–(h). The DDR boundary was finally determined with the contour level of $\beta = 0.92$. When the DDR is approximated as an ellipse, its spatial extent was estimated as the magnitudes of the long and short axes of the ellipse. As a result, along the north–south and east–west directions, the spatial extents of DDR are ∼75 and ∼80 m, respectively. The determined boundary is shown in Fig. 6(b) as the red dashed line.,

Following the same method described above, the spatial extent of the FDR was also determined by a set of contour levels defined as $\beta = \{0.85,\ 0.83\ 0.82\ 0.80,\ 0.78\}$. The method of determining elements in β is the same as it utilized in the above DDR boundary determination. The process of the DDR boundary determination is shown in Fig. 5. From Fig. 5(a) to (d), the isolines were drawn with contour levels of $\beta_1 = \{0.85,\ 0.83\ 0.82\ 0.80,\ 0.78\}$, $\beta_2 = \{0.83\ 0.82\ 0.80,\ 0.78\}$, $\beta_3 = \{0.82\ 0.80,\ 0.78\}$, and $\beta_4 = \{0.80,\ 0.78\}$, respectively. Based on the spatial distribution changes of these isoline graphs, the FDR boundary, marked as a green ellipse in Fig. 3, finally

corresponded to the contour level of $\beta = 0.82$. The spatial extent of the FDR was estimated as ∼9.6 m in the north–south direction and ∼10.8 m in the east–west. When the FDR is approximated as an ellipse, its spatial extent was estimated as ∼9.6 m and ∼10.8 m, respectively, along the north–south and east–west directions. The determined boundary is shown in Fig. 6(b) as the green dashed line.,

3) Final Determination of Spatial Extents of FDR and DDR: Comparing the results derived from the reflectance isoline graphs with the results of the reflectance profiles, the spatial extent estimation for the FDR was consistent with a difference of ≤1 m. While for the DDR, the estimation of the spatial extent had a larger difference of ∼10 m. We also found that for reflectance profiles themselves, there was a ∼16 m difference along the west–east direction. The reason for this difference is that the performance of the reflectance profiles was affected by noise (including topographical factors and register errors).

In fact, the difference in I/F ratio value between DDR and UDR is generally <0.002 (can be found in Section III-B), therefore, boundary determination by using a single direction-based reflectance profile can easily overlook such small differences. As a result, it is possible that the DDR determined by the reflectance profile is less than the true spatial extent of DDR.

While for reflectance isoline graphs, they are composed of a set of isolines, and each of these contours corresponds to a specific ratio value of the temporal-ratio image. Reflectance isoline graphs are finely combining the change of reflectance and the spatial information. The integration of the spatial distribution information of groups of I/F ratio isolines can undoubtedly
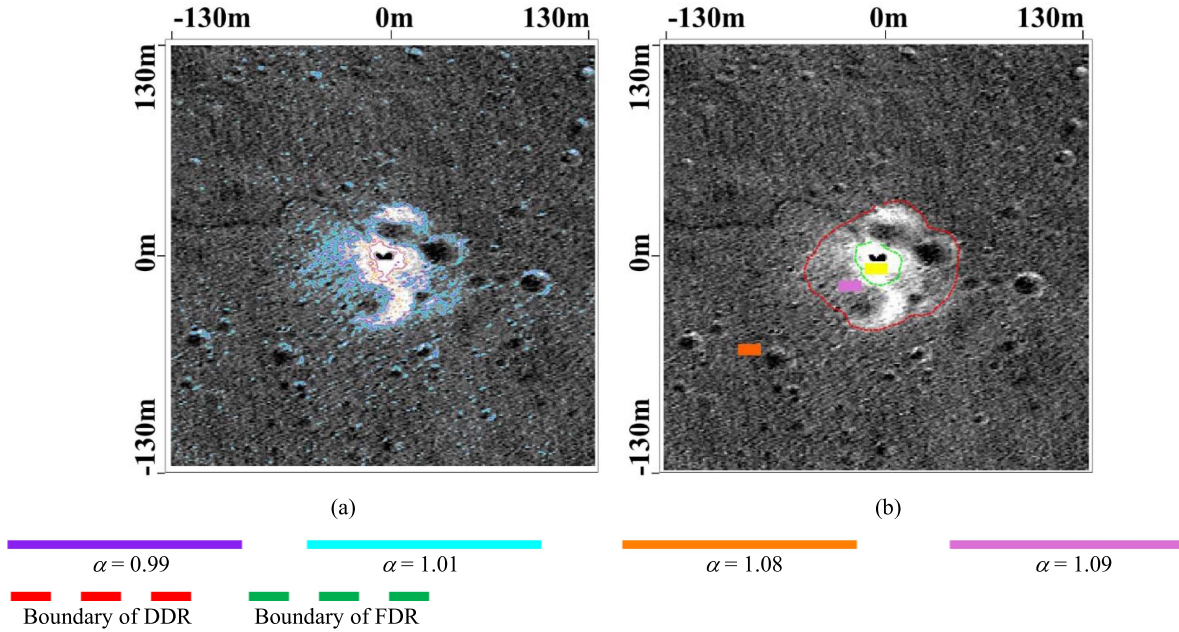
Fig. 6. (a) Reflectance isoline graph overlaid on the temporal-ratio image. (b) Final determination of the spatial extent of the DDR (red polyline) and FDR (green polyline) determined by the reflectance isoline graph. Some representative patches of the UDR, the DDR, and the FDR were selected for average I/F values calculated in Section III-B. These patches are respectively labeled as orange, pink, and yellow rectangles in Fig. 3(b).

enhance the robustness to noise. Therefore, we considered that the spatial extent of DDR determined by reflectance isoline graphs is more robust.

The final determination of the spatial extent of the engine exhaust disturbed region is shown in Fig. 6. The FDR was ∼9.6 m in the north–south direction and ∼10.8 m in the east–west direction. The DDR was of ∼75 and ∼85 m along the north–south and east–west directions, respectively. The boundary of DDR and FDR are respectively outlined by red polyline and green polyline.

B. Reflectance Variation of the Engine Exhaust-Disturbed Region

In the phase-ratio image, the disturbed region was presented as a darker spot, showing that the disturbed regolith reflectance viewed at a large phase angle had increased, which was contrary to the theoretical law of phase function described and thus assumed to be a photometric anomaly.

Based on the determined spatial extent of the UDR, the DDR, and the FDR, the I/F values of these regions were obtained and compared. In the NAC image pair for the phase-ratio image, some representative regions of the UDR, the DDR, and the FDR were selected, and the I/F values of these regions were averaged for comparison. These regions were labeled as green, orange, and magenta rectangles in Fig. 3(a), and the corresponding averaged I/F values for each image are shown in Table III.

With an incidence angle of approximately 46.0°, the image with the large phase angle of 47.4° (M1372969744R) had a lower I/F value than that of M1314237625L with a phase angle of 16°, on the whole, and a magnitude of ∼2.5%. As presented in Table III, image M1372969744R had a ∼3% higher I/F value

TABLE III
THE AVERAGED I/F VALUES OF THE UDR, THE FDR, AND THE DDR FOR THE SELECTED NAC IMAGES

Image ID	UDR	DDR	FDR
M1372969744R	0.044	0.046	0.050
M1314237625L	0.070	0.072	0.076

for the FDR than for the DDR, and the I/F value of the DDR was also ∼2% higher than the UDR. For image M1314237625L, similar results were achieved.

For temporal images, the I/F ratio of the background (i.e., the UDR) should be 1.0, theoretically, if no photometric change existed. However, practical factors, such as the difference in the geometric properties and the matching errors of the images before and after landing, could have had an impact on the ratio images. In this article, the I/F ratio of the background determined by using reflectance files was 0.99; however, when using the isoline graph, the I/F ratio of the background was estimated as 0.96. As the performance of the reflectance profiles was easily affected by terrain factors, we used the result of the isoline graph to perform the final estimation. Based on the isoline graph, the I/F ratio of 0.93 was used to distinguish the UDR and the DDR, and the I/F ratio of 0.8 was used to distinguish the DDR and the FDR.

IV. DISCUSSION

A. Analysis of the Performance of the Reflectance Isoline Graphs

The spatial extent of the decent engine exhaust disturbed region by Chang'E-3 spacecraft was carefully studied [8]. In their study, reflectance profiles taken across the landing site
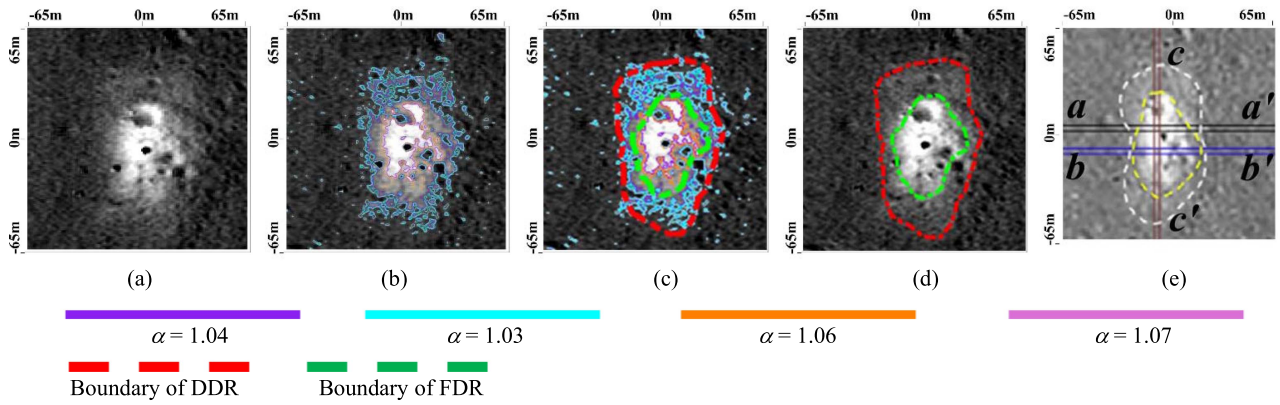
Fig. 7. (a) Temporal-ratio image made by dividing the NAC image M1144936321L after landing by image M183661683L before landing. (b) Reflectance isolines graph derived from temporal-ratio image(a), with contours = 1.04,1.03, 1.06, 1.07. (c) The spatial extents of DDR(DBZ) and FDR(FBZ) determined by Clegg et al.(2016) by using reflectance profiles. The yellow and white dashed line respectively outline the DDR and FDR. (d) Spatial extents of DDR and FDR determined by proposed reflectance isoline graphs. The green and red dashed line respectively outline the FDR and DDR.

based on the temporal ratio image delimit the spatial extent of the disturbed region. The used profiles are shown in Fig. 7(c) as a-a', b-b', and c-c'. The final determined result is also shown in Fig. 7(c), where the yellow and white dashed lines respectively outline the FDR and DDR in their paper, they are respectively called focused blast zone (FBZ) and diffused blast zone (DBZ)[. The FBZ is ∼75 m elongated in the N–S direction, and ∼43 m E–W at the maximum width of an irregular shape. The DBZ extended ∼40–50 m from the edge of the FBZ in the N–S direction and ∼10–15 m in the E–W direction.

To evaluate the performance of the reflectance isoline graphs, we utilized the isoline graphs to determine the spatial boundaries of FDR and DDR of Chang'E-3 engine exhaust disturbed, and then compared the result with Clegg's results. To determine the FDR spatial extent, a set of contour levels β = {1.0, 1.01, 1.02 1.03,1.04} were used. To determine the DDR spatial extent, β = {1.04, 1.05, 1.06 1.07,1.08} were used. The final determined spatial extents of FDR and DDR are respectively outlined by red and green lines as shown in Fig. 7(d). The FDR was ∼75.5 m in the north–south direction and ∼42 m in the east–west direction for the widest part. From the edge of FDR, the DDR extended by ∼50 and ∼15 m along the north–south and east–west directions, respectively.

Comparing these results, it can find that the spatial extent estimation for the DDR was consistent with a difference of ≤1 m. For the DDR, the estimation of the spatial extent had a difference of ∼0–5 m. Comparing Fig. 7(c) and (d), it can find that around the determined DDRs with the largest difference (∼5 m) of these two methods, there clustered a lot of small craters. In this way, it can be assumed that it is mainly topographic factors that cause the difference between the two determination boundaries.

According to the Fig. 7(d), we can see that the part of the two results with a larger DDR difference (∼5 m) has more small impact craters around it, so it can be assumed that it is mainly topographic factors that cause the difference between the two determination boundaries. In fact, since there is no real reference value, we cannot precisely state which result is more accurate. However, our results are generally in agreement with those of

Clegg's, therefore, it is reasonable to consider the reflectance isoline graphs as a reliable tool to determine the spatial extent of the engine exhaust disturbed region for both FDR and DDR.

B. Analysis of the Size and Shape of the Disturbed Region

The final estimated spatial extent of the DDR for Chang'E-4 landing site was ∼75 m along the north–south direction and ∼80 m along the east–west direction. While the spatial extent of the FDR was estimated at ∼9.6 m along the north–south direction and ∼10.8 m along the east–west direction. According to Clegg's work [10], DDR for Chang'E-3 landing site was estimated at ∼75 m along the north–south direction and ∼43 m along the east–west direction. The spatial extent of the FDR was estimated at ∼40–50 m along the north–south direction and ∼10–15 m along the east–west direction. Comparing these results, we found that the spatial extent of the FDR of the Chang'E-4 landing site was smaller than that of the Chang'E-3 while the spatial extent of the DDR of the Chang'E-4 landing site was larger. Considering that the mass and thrust of the Chang'E-3 and Chang'E-4 landers were almost the same [26], [27], in terms of FDR, we considered the possible reason for this difference could lie in the image resolution. According to Clegg's work [10], due to the resolution of the image they used (the image was 1.5 m/pixel), a smaller disturbed region could be finely determined. In this study, all the NAC images had a resolution of ∼0.8 m/pixel. As for the difference in the spatial extent of the DDR, we considered the possible reasons could lie in the differences in the topography and geology between these two landing sites.

The Chang'E-3 landing site was located in the Imbrium basin on the basalts, which was estimated as Eratosthenian in age. They represented some of the youngest lunar units at approximately 2.35–2.5 billion years (Gy) old [28]. The Chang'E-4 landing site was located in the Von Kármán crater, whose geologic age was estimated at approximately 3.6Ga [29]. As compared to Chang'E-3, the Chang'E-4 landing site had experienced a long history of space weathering caused by solar winds,
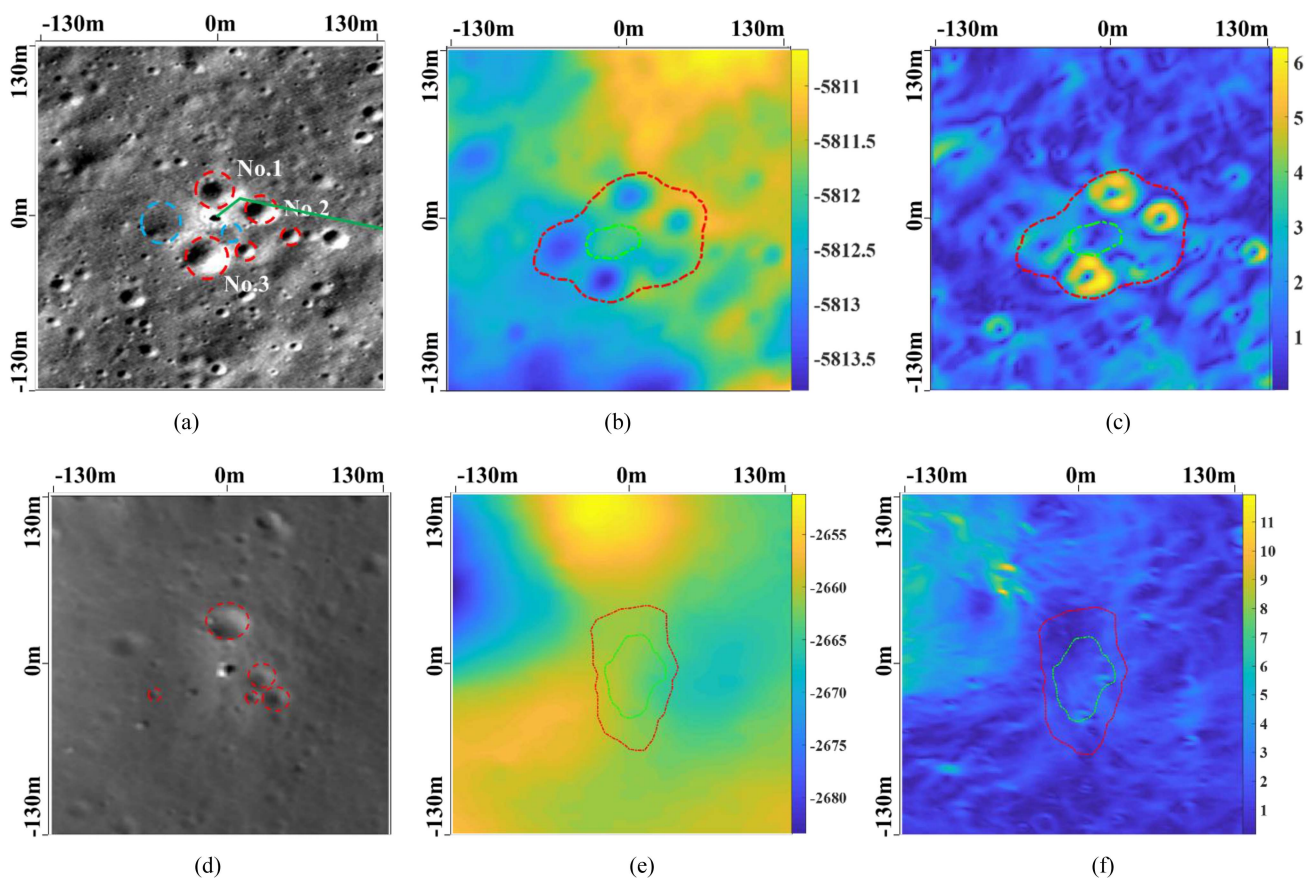
Fig. 8. Topographic factors of the Chang'E-4 and Chang'E-3 landing sites. (a) Craters and low-lying regions around the Chang'E-4 landing site. The red circles denote craters, the blue circles denote low-lying regions, and the green line denotes the flight trajectory of the Chang'E-4 spacecraft. (b) DEM of the Chang'E-4 landing site and determined boundaries of DDR and FDR are overplayed on. (c) Slope map of the Chang'E-4 landing site and determined boundaries of DDR and FDR are overplayed on. (d) Craters around the Chang'E-3 landing site. (e) DEM of the Chang'E-3 landing site and determined boundaries of DDR and FDR are overplayed on. (f) Slope map of the Chang'E-3 landing site and determined boundaries of DDR and FDR are overplayed on.

galactic cosmic rays, micrometeorites, and larger meteors [30], [31], and, thus, a fine-grained, porous regolith layer could exist. This was partially verified by the panoramic camera images obtained by the Chang'E-3 and Chang'E-4 rovers. Additionally, observations from the lunar penetrating radar showed that the thickness of the regolith at the Chang'E-4 landing site was constrained at ~12 m, which was approximately 1.3–3 times thicker than the Chang'E-3 landing site [32]. As a result, a larger amount of the regolith could be affected by the engine exhaust, thus the area of FDR surrounding the Chang'E-4 landing site was expected to be larger than that of the Chang'E-3, which was agreed with our findings in this study.

The digital elevation model (DEM) of the Chang'E-4 landing site with a spatial resolution of 2 m/pixel was created by using shape-from-shading [21], and the slope map was calculated according to the DEM. The DEM and slope map are shown in Fig. 8(b) and (c), respectively. According to Liu's work [19], the Chang'E-4 spacecraft landed on a gentle slope that was approximately 3°. Around the landing site, there were five craters with diameters of 10.21–25.00 m and depths of 1.21–3.03 m. As shown in Fig. 8(a), these five craters were numbered according to their distance from the landing site and labeled as red dotted lines. The first crater had a diameter of 25 m and a depth of 3.03

m, and it was only 8.35 m to the north of the landing site, while the second crater was approximately 16.07 m away from the lander, with a diameter of 18.75 m and a depth of 1.90 m. The third crater was approximately 25.05 m away from the lander with a diameter of 25.00 m and a depth of 2.78 m. In addition, there were also two shallow low-lying areas with diameters of ~35 and ~23 m in the west and southeast of the landing site, respectively. These shallow low-lying areas were labeled as blue dotted lines. As Fig. 8(b) and (c) show, at approximately ~50 m around the lander, the surface slope changed to < 7°, and the elevation changed to < 3 m. According to Clegg's work [10], such minor changes in local topology would not influence the normalized surface reflectance values, based on a Hapke model evaluation. However, the craters may have acted as a mechanism to influence the size and shape of the spatial extent of the disturbed region.

Based on our study, the craters and shallow low-lying areas acted as a container enlarging the spatial extent of the disturbed region, which was consistent with previous studies [4], [10]. These suggested that craters or low-lying areas had played a role in containing rocket exhaust and thus had led the entire crater or low-lying areas to be more significantly disturbed than the flat regions. In this way, one of the possible reasons why the

TABLE IV
NORMALIZED REFLECTANCE OF UDR, FDR, AND DDR FOR THE SELECTED
NAC IMAGES

Image ID	UDR	DDR	FDR
M1372969744R	0.031	0.032	0.034
M1314237625L	0.042	0.043	0.049

shape of Chang'E-4's DDR space range is close to a circle is that the craters and shallow low-lying areas around the lander are at about the same distance from it. In particular, according to the topography of the Chang'E-4 landing region, there is a low-lying area with a diameter of about 25 m in the southeast of the lander. Based on the above conclusion, this indicates that the low-lying area has an effect on enlarging the disturbed region. Therefore, it is reasonable that the disturbance range along the east-west direction of the Chang'E-4 landing site is larger than it is of the Chang'E-3 landing site.

The spatial extent along the north–south direction of the Chang'E-3 landing site was much larger than along the west–east direction. This may have been caused by the spacecraft hovering at an altitude of 100 m above the lunar surface. At an altitude of 100 m, the Chang'E-3 lander was first moved southward at a distance of 6 m, and in this process, the fine particles of the regolith may have been redistributed [6], [18]. However, the flight trajectory of Chang'E-4 spacecraft disputed this argument. For the Chang'E-4 landing mission, the spacecraft had hovered for ~13 s at an altitude of 99 m and then moved 12 m to the southwest for the final landing [19]. However, according to the results derived from either the phase-ratio image or the temporal image, there was no evidence of a disturbed elongated region in this direction.

According to You's work [33], a plume-dust interaction and a wind erosion model for the Chang'E-4 landing were simulated with a computational fluid dynamics software. It denoted that when the elevation of the lander was approximately 13.5 m, the change in the image DN level could be observed from the landing camera (LCAM) images, and the eroded radius (defined from the center of the lander) of this elevation was approximately 9 m. When the lander descended, the radius decreased, but the erosion pressure was also more intense. Since the Chang'E-4 was the backup of Chang'E-3, they had similar dry mass; therefore, we inferred the radius of the FDR was also approximately 9 m, as the Chang'E-3 FDR had been, which coincided with the results derived by the isoline graph.

C. Analysis of the Reflectance Values of the Disturbed Region

For a quantitative comparison of the variations in the reflectance values between the UDR, the DDR, and the FDR of the Chang'E-3 and Chang'E-4 landing sites, an empirical global photometric solution was used to photometrically normalize the selected NAC images at the pixel scale with an illumination condition of $i = 30°$, $e = 0°$, and $\alpha = 30°$ [10], [34]. The representative regions of the UDR, the DDR, and the FDR were the same as described in Section III-A, as shown in Fig. 6(a). The corresponding normalized reflectance values for each image are shown in Table IV. The normalized reflectance of the UDR was the lowest, and for DDR, it was the highest, indicating the surface of the disturbed area was smoother than that of the UDR. For each image, the normalized reflectance value of the DDR was ~3% higher than that of the FDR, and the I/F value of the FDR was also ~2% higher than that of the UDR. Comparing the normalized reflectance of the DDR and the UDR, it increased to ~9.4% for NAC image M1372969744R and increased to ~7.5% for NAC image M1314237625L; both results were consistent with previous studies [6], [7].

The increased brightness of the lunar surface, which was essentially the decrease of the phase-function slope, was due to the weakening of the shadow effect [10], [35]. The lander engine exhaust had impacted the lunar surface, resulting in rapid surface dust transportation and surface erosion [35], and could explain the photometric anomalies presented at the landing site. As shown in the LCAM images in Fig. 9, from (a) to (b), the reflectance of the image gradually increased, and in (c) and (d), the dust motion could clearly be observed. This dust-blowing process may have destroyed the porous "fairy castle" structure of the superficial regolith and thus weakened the shadowing effect of the regolith. At the same time, the engine exhaust gases had exerted significant pressure on the regolith, so in addition to blowing the topmost regolith away, they may also have compacted the remaining soil more tightly on micron/millimeter scales. According to some experimental and computer models studying the entrainment of lunar particles in high-velocity gases, the smaller particles with a size of nm~ μm had been rapidly entrained and accelerated to high velocities by the rocket engine exhaust and then had been redistributed farther away from the lander [36], [37], [38]. By further considering the turbulence and particle–particle collisions, some of the particles would be slowed and redistributed within 10–100 m [38]. This could partly explain why the reflectance of the disturbed region was less bright.

In addition, as shown in LROC NAC image M1370616052 and image M1311893667 in Fig. 2, the reflectance of the FDR increased while the reflectance of the rover track decreased. In the phase-ratio image, the FDR was translated as a dark spot while the rover track was highlighted as a bright curve. As a result, we considered the disturbance mechanism of the engine exhaust and the rover to the lunar regolith to be the opposite. If the engine exhaust decreased the backscattering of the landing site, then the rover led to more forward scattering in the track. In the Chang'E-4 mission, some in situ data were collected, as shown in Fig. 10(a). The N001, N003, and N004 were three observation sites. The N001 was located in the FDR. The N003 and the N004 were remarkably close to each other, and both were located in the DDR. In the temporal image and its isoline graph, as shown in Fig. 10(b) and (c), the engine exhaust disturbed trace of the N001 was evident while the disturbed traces of the regions surrounding the N003 and the N004 were not as obvious. In addition to the topographic factors mentioned in Section IV-B, there was another factor that could have influenced the interaction between the engine exhaust and the rover's wheel. Since the effects of these two operations on the regolith photometry were opposite, the reflectance anomaly presented on the temporal image was smoothed.
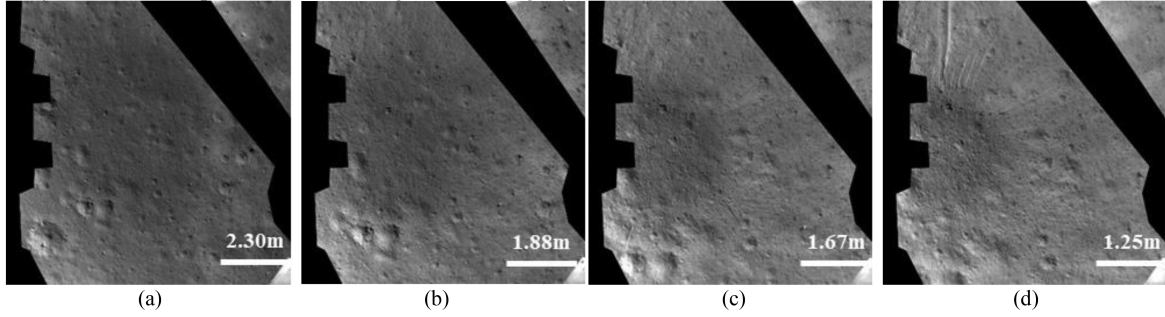
Fig. 9.   Landing camera images of the Chang'E-4 landing site in which the disturbance of the engine exhaust to the regolith can be clearly observed. Images were captured at an altitude of approximately (a) 11 m, (b) 9 m, (c) 8 m, and (d) 6 m. From (a) to (b), the reflectance of the images gradually increases. In images (c) and (d), the dust blowing can be clearly observed.
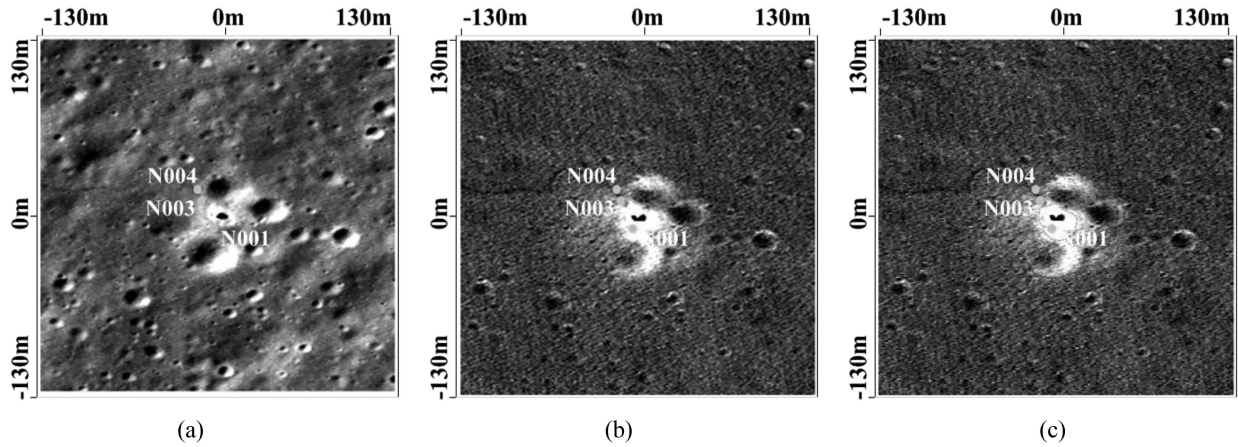

Fig. 10.   The in situ observation sites N001, N003, and N004 are labeled in images. (a) NAC image M1372969744 with N001, N003, and N004. (b) Temporal image with N001, N003, and N004. (c) Spatial extent of DDR and FDR with the N001, N003, and N004.

V. CONCLUSION

In this study, the photometric anomalies induced by the spacecraft's engine exhaust at the Chang'E-4 landing site were detected and analyzed. By using phase-ratio and temporal-ratio images, the disturbed areas were determined. By further combining the reflectance isoline graphs and the reflectance profiles, the spatial extents and the reflectance changes of the disturbed regions were quantitatively determined. In particular, the reflectance isoline graph was an effective and robust tool to quantitatively determine the spatial range of the engine exhaust-disturbed region for the first time in current research. The reflectance isoline graphs are composed of a set of isolines, and each of these contours corresponds to a specific ratio value of the temporal-ratio image. Reflectance isoline graphs are finely combining the change of reflectance and the spatial information. The integration of the spatial distribution information of groups of I/F ratio isolines can undoubtedly enhance the robustness to noise. Therefore, we considered that the spatial extent of DDR determined by reflectance isoline graphs is more robust. In addition, based on various contour levels, the DDR and the FDR were accurately distinguished.

The final estimation of the spatial extent of the DDR for the Chang'E-4 landing site was ∼75 and ∼80 m along the north–south and east–west directions, respectively. The spatial extent of the FDR was estimated at ∼9.6 and ∼10.8 m along the north–south and the east–west directions. The estimated spatial extent of the FDR was consistent with the results derived from a plume-dust interaction and wind erosion model. As a result, the isoline graph was proven to be an effective tool in dividing and determining the spatial extent of various disturbed regions.

As compared with the engine exhaust-disturbed region of the Chang'E-3 landing site, the Chang'E-4 landing rocket engine exhaust-disturbed region was larger. We reached this conclusion as the craters and shallow low-lying areas around the landing point had acted as containers and enlarged the spatial extent of the disturbed region. Meanwhile, the long duration of the space weathering effect may have also played an important role by forming a fine, porous regolith layer that could be easily blown away.

Hovering at an altitude of ∼100 m above the lunar surface, the Chang'E-3 spacecraft had an impact on the spatial extent of the disturbed region, particularly in the north–south direction. However, based on the flight trajectory of the Chang'E-4 spacecraft and our estimated spatial extent of the DDR, such a conclusion could not be supported.

In the phase-ratio image, the engine exhaust-disturbed region was shown as a dark spot while the rover track was highlighted

as a bright curve. Therefore, we determined that the disturbances caused by the engine exhaust and the rover's wheel to the lunar regolith were opposite in nature. The in situ observation sites of Chang'E-4 N001, N003, and N004, were included in the estimated engine exhaust-disturbed region. It was necessary to consider the disturbance effect when analyzing local spectral features.

As compared to the photometry analysis of the Chang'E-3 landing site, the reflectance changes around the Chang'E-4 landing site were similar. The possible reasons for the increased reflectance in the disturbed area of the images after landing were as follows:

1) the engine exhaust blew away the top layer of particles and smoothed the surface;
2) the engine exhaust destroyed the fairy-castle structure;
3) a combination of these two processes.

ACKNOWLEDGMENT

REFERENCES

[1] B. Hapke, "Bidirectional reflectance spectroscopy: 1. Theory," *J. Geophys. Res., Solid Earth*, vol. 86, no. NB4, pp. 3039–3054, Apr. 1981.

[2] V. Kaydash et al., "Photometric anomalies of the lunar surface studied with SMART-1 AMIE data," *Icarus*, vol. 202, no. 2, pp. 393–413, Aug. 2009.

[3] B. Hapke, *Theory of Reflectance and Emittance Spectroscopy*. Cambridge, U.K.: Cambridge Univ. Press, 2012.

[4] Y. Yang, S. Li, R. E. Milliken, H. Zhang, K. Robertson, and T. Hiroi, "Phase functions of typical lunar surface minerals derived for the Hapke model and implications for visible to near-infrared spectral unmixing," *J. Geophysical Res., Planets*, vol. 124, no. 1, pp. 31–60, Jan. 2019.

[5] V. Kaydash, Y. Shkuratov, V. Korokhin, and G. Videen, "Photometric anomalies in the Apollo landing sites as seen from the Lunar reconnaissance orbiter," *Icarus*, vol. 211, no. 1, pp. 89–96, Jan. 2011.

[6] M. A. Kreslavsky and Y. G. Shkuratov, "Photometric anomalies of the lunar surface: Results from clementine data," *J. Geophysical Res., Planets*, vol. 108, no. E3, Mar. 2003.

[7] R. N. Clegg, B. L. Jolliff, M. S. Robinson, B. W. Hapke, and J. B. Plescia, "Effects of rocket exhaust on lunar soil reflectance properties," *Icarus*, vol. 227, no. SI, pp. 176–194, Jan. 2014.

[8] Y. Wu and B. Hapke, "Spectroscopic observations of the Moon at the lunar surface," *Earth Planet. Sci. Lett.*, vol. 484, no. 15, pp. 145–153, Feb. 2018.

[9] Y. Wu, Z. Wang, and Y. Lu, "Space weathering of the Moon from in situ detection," *Res. Astron. Astrophys.*, vol. 19, no. 4, May 2019, Art. no. 051.

[10] R. N. Clegg-Watkins et al., "Photometric characterization of the Chang'e–3 landing site using LROC NAC images," *Icarus*, vol. 273, no. SI, pp. 84–95, Jul. 2016.

[11] H. Sato, M. S. Robinson, B. Hapke, B. W. Denevi, and A. K. Boyd, "Resolved Hapke parameter maps of the Moon," *J. Geophysical Res., Planets*, vol. 119, no. 8, pp. 1775–1805, Aug. 2014.

[12] H. Lin et al., "In situ photometric experiment of lunar regolith with visible and near-infrared imaging spectrometer on board the Yutu-2 lunar rover," *J. Geophysical Res., Planets*, vol. 125, no. 2, Feb. 2020, Art. no. e2019JE006076.

[13] T. Y. Xu, B. Hapke, X. P. Zhang, Y. Wu, and X. P. Lu, "Spectrophotometry of the lunar regolith using the Chang'e–3 panoramic camera (PCAM)," *Astron. Astrophys.*, vol. 665, Sep. 2022, Art. no. A15.

[14] Y. Wang, Z. Xiao, Y. Chang, and J. Cui, "Lost volatiles during the formation of hollows on Mercury," *J. Geophysical Res., Planets*, vol. 125, no. 9, Aug. 2020, Art. no. e2020JE006559.

[15] T. Jiang et al., "In situ lunar phase curves measured by Chang'e–4 in the Von Kármán Crater, South Pole-Aitken basin," *Astron. Astrophys.*, vol. 646, no. A2, pp. 1–15, Jan. 2021.

[16] H. Zhang et al., "In situ optical measurements of Chang'e–3 landing site in Mare Imbrium: 1. Mineral abundances inferred from spectral reflectance," *Geophysical Res. Lett.*, vol. 42, no. 17, pp. 6945–6950, Sep. 2015.

[17] H. Lin et al., "New insight into lunar regolith-forming processes by the lunar rover Yutu-2," *Geophysical Res. Lett.*, vol. 47, no. 14, Jul. 2020, Art. no. e2020GL087949.

[18] Z. Tang et al., "Physical and mechanical characteristics of lunar soil at the Chang'e–4 landing site," *Geophysical Res. Lett.*, vol. 47, no. 22, Nov. 2020, Art. no. e2020GL089499.

[19] J. Liu et al., "Descent trajectory reconstruction and landing site positioning of Chang'e–4 on the lunar farside," *Nature Commun.*, vol. 10, no. 1, Nov. 2019, Art. no. 4229.

[20] J. A. Anderson, S. C. Sides, D. L. Soltesz, T. L. Sucharski, and K. J. Becker, "Modernization of the integrated software for imagers and spectrometers Lunar Planet," in *Proc. Lunar and Planet. Sci. Conf.*, no. 1777, 2004, pp. 2039–2043.

[21] O. Alexandrov and R. A. Beyer, "Multiview shape-from-shading for planetary images," *Earth Space Sci.*, vol. 5, no. 10, pp. 652–666, Oct. 2018.

[22] J. N. Sarvaiya, S. Patnaik, and S. Bombaywala, "Image registration by template matching using normalized cross-correlation," in *Proc. Adv. Comput., Control, Telecommun. Technol. Conf.*, 2009, pp. 819–822.

[23] M. S. Robinson et al., "Lunar reconnaissance orbiter camera (LROC) instrument overview," *Space Sci. Rev.*, vol. 150, no. 1, pp. 81–124, Jan. 2010.

[24] P. T. Metzger, J. Smith, and J. E. Lane, "Phenomenology of soil erosion due to rocket exhaust on the Moon and the Mauna Kea lunar test site," *J. Geophysical Res., Planets*, vol. 116, no. E6, Jun. 2011, Art. no. E06005.

[25] Y. Shkuratov, V. Kaydash, V. Korokhin, Y. Velikodsky, N. Opanasenko, and G. Videen, "Optical measurements of the Moon as a tool to study its surface," *Planet. Space Sci.*, vol. 59, no. 13, pp. 1326–1371, Oct. 2011.

[26] C. Li et al., "The Chang'e-3 mission overview," *Space Sci. Rev.*, vol. 190, no. 1, pp. 85–101, Jun. 2015.

[27] Y. Jia, Y. Zou, J. Ping, C. Xue, J. Yan, and Y. Ning, "The scientific objectives and payloads of Chang'E– 4 mission," *Planet. Space Sci.*, vol. 162, pp. 207–215, Nov. 2018.

[28] C. Ding et al., "Layering structures in the porous material beneath the Chang'e–3 landing site," *Earth Space Sci.*, vol. 7, no. 10, May 2020, Art. no. e2019EA000862.

[29] J. Huang et al., "Geological characteristics of Von kármán Crater, Northwestern South Pole-Aitken basin: Chang'E–4 landing site region," *J. Geophysical Res.: Planets*, vol. 123, no. 7, pp. 1684–1700, Jul. 2018.

[30] S. Gou et al., "In situ spectral measurements of space weathering by Chang'e–4 rover," *Earth Planet. Sci. Lett.*, vol. 535, Apr. 2020, Art. no. 116117.

[31] P. Luo, X. Zhang, S. Fu, Y. Li, C. Li, and J. Cao, "First measurements of low-energy cosmic rays on the surface of the lunar farside from Chang'e–4 mission," *Sci. Adv.*, vol. 8, no. 2, May 2022, Art. no. eabk1760.

[32] Z. Dong, G. Fang, B. Zhou, D. Zhao, Y. Gao, and Y. Ji, "Properties of Lunar regolith on the Moon's farside unveiled by Chang'e–4 Lunar penetrating radar," *J. Geophysical Res., Planets*, vol. 126, no. 6, Jul. 2021, Art. no. e2020JE006564.

[33] J. You et al., "Analysis of plume–lunar surface interaction and soil erosion during the Chang'e–4 landing process," *Acta Astronautica*, vol. 185, pp. 337–351, Aug. 2021.

[34] A. K. Boyd, J. D. Stopar, and M. S. Robinson, "LROC NAC photometric analysis: A global solution and local applications," in *Proc. Lunar Planet. Sci. Conf.*, 2014, no. 1777, Art. no. 2826.

[35] B. Hapke, "Bidirectional reflectance spectroscopy 7: The single particle phase function hockey stick relation," *Icarus*, vol. 221, no. 2, pp. 1079–1083, Nov./Dec. 2012.

[36] P. T. Metzger, S. Jacob, and E. L. John E., "Phenomenology of soil erosion due to rocket exhaust on the Moon and the Mauna Kea Lunar test site," *J. Geophysical Res., Planets*, vol. 116, no. E6, pp. 1–22, Sep. 2011.

[37] K. J. Berger, A. Anand, P. T. Metzger, and C. M. Hrenya, "Role of collisions in erosion of regolith during a Lunar landing," *Phys. Rev. E*, vol. 87, no. 2, Oct. 2013, Art. no. 022205.

[38] A. B. Morris, D. B. Goldstein, P. L. Varghese, and L. M. Trafton, "Approach for modeling rocket plume impingement and dust dispersal on the Moon," *J. Spacecraft Rockets*, vol. 52, no. 2, pp. 362–374, Jun. 2015.

Yaqiong Wang received the B.S. and M.S. degrees in electronic engineering from Liaoning Technical University, Fuxin, China, in 2016 and 2018, respectively. She is currently working toward the Ph.D. degree in photogrammetry and remote sensing from Tongji University, Shanghai, China.

Her research interests include image processing for high-resolution remote sensing and its applications.

Xiaohua Tong (Senior Member, IEEE) received the Ph.D. degree in traffic engineering from Tongji University, Shanghai, China, in 1999.

From 2001 to 2003, he was a Postdoctoral Researcher with the State Key Laboratory of Information Engineering in Surveying, Mapping, and Remote Sensing, Wuhan University, Wuhan, China. He was a Research Fellow with Hong Kong Polytechnic University, Hong Kong, in 2006, and a Visiting Scholar with the University of California, Santa Barbara, CA, USA, from 2008 to 2009. His research interests include photogrammetry and remote sensing, trust in spatial data, and image processing for high-resolution satellite images.

Huan Xie (Senior Member, IEEE) received the B.S. degree in surveying engineering, and the M.S. and Ph.D. degrees in cartography and geoinformation from Tongji University, Shanghai, China, in 2003, 2006, and 2009, respectively.

From 2007 to 2008, she was with the Institute of Photogrammetry and GeoInformation, Leibniz Universität Hannover, Germany, funded by the China Scholarship Council, as a Visiting Scholar. Her research interests include satellite laser altimetry and hyperspectral remote sensing.

Sicong Liu (Member, IEEE) received the B.Sc. degree in geographical information system and the M.E. degree in photogrammetry and remote sensing from the China University of Mining and Technology, Xuzhou, China, in 2009 and 2011, respectively, and the Ph.D. degree in information and communication technology from the University of Trento, Trento, Italy, in 2015.

He is currently an Associate Professor with the College of Surveying and Geo-Informatics, Tongji University, Shanghai, China. His research interests include multitemporal data analysis, change detection, multispectral/hyperspectral remote sensing and planetary remote sensing.

Dr. Liu was the winner (ranked as third place) of Paper Contest of the 2014 IEEE GRSS Data Fusion Contest. He is the Technical Co-Chair of the Tenth International Workshop on the Analysis of Multitemporal Remote Sensing Images (MultiTemp 2019). He serves as the Program Committee Member for SPIE Remote Sensing Symposium: Image and Signal Processing for Remote Sensing XXVI–XXVIII (2020–2022), and also served as the Session Chair for many international conferences such as International Geoscience and Remote Sensing Symposium (2017–2019). He is/was a Guest Editor for the IEEE JOURNAL OF SELECTED TOPICS IN APPLIED EARTH OBSERVATIONS AND REMOTE SENSING (JSTARS) and *Remote Sensing*.

Chao Wang received the B.S. degree in remote sensing and geography information system from China University of Mining and Technology, Jiangsu, China, in 2010, and the Ph.D. degree in cartography and geography information system from East China Normal University, Shanghai, China, in 2016.

From 2014 to 2016, he was with the Laboratoire de Météorologie Dynamique/IPSL, CNRS, Sorbonne Université, Paris, France, funded by the China Scholarship Council, as a joint Ph.D. student. He is currently an Assistant Professor with Tongji University, Shanghai, China. His research interests include hyperspectral remote sensing, and planetary atmosphere.

Xiong Xu (Member, IEEE) received the B.Sc. degree in photogrammetry and the Ph.D. degree in photogrammetry and remote sensing from Wuhan University, Wuhan, China, in 2008 and 2013, respectively.

He was a Postdoctoral Researcher with Prof. Antonio Plaza (IEEE Fellow) between 2014 and 2017. He is currently an Associate Professor with the College of Surveying and Geoinformatics, Tongji University, Shanghai, China. His current research interests include multi- and hyperspectral image processing, deep learning in remote sensing, and remote sensing applications.